

Shock Waves in a Superfluid with Higher-Order Dispersion

M. E. Mossman,¹ E. S. Delikatny,¹ Michael McNeil Forbes,^{1,2,*} and P. Engels^{1,†}

¹*Department of Physics and Astronomy, Washington State University, Pullman, WA, USA 99164*

²*Department of Physics, University of Washington, Seattle, WA 98105, USA*

Higher-order dispersion can lead to intriguing dynamics that are becoming a focus of modern hydrodynamics research. Such systems occur naturally, for example in shallow water waves and nonlinear optics, for which several types of novel dispersive shocks structures have been identified. Here we introduce ultracold atoms as a tunable quantum simulations platform for higher-order systems. Degenerate quantum gases are well controlled model systems for the experimental study of dispersive hydrodynamics in superfluids and have been used to investigate phenomena such as vortices, solitons, dispersive shock waves and quantum turbulence. With the advent of Raman-induced spin-orbit coupling, the dispersion of a dilute gas Bose-Einstein condensate can be modified in a flexible way, allowing for detailed investigations of higher-order dispersion dynamics. Here we present a combined experimental and theoretical study of shock structures generated in such a system. The breaking of Galilean invariance by the spin-orbit coupling allows two different types of shock structures to emerge simultaneously in a single system. Numerical simulations suggest that the behavior of these shock structures is affected by interactions with vortices in a manner reminiscent of emerging viscous hydrodynamics due to an underlying quantum turbulence in the system. This result suggests that spin-orbit coupling can be used as a powerful means to tune the effective viscosity in cold-atom experiments serving as quantum simulators of turbulent hydrodynamics, with applications from condensed matter and optics to quantum simulations of neutron stars.

The dynamics of systems with higher-order dispersion is currently at the forefront of modern hydrodynamics research. While systems with parabolic dispersion are well understood, higher-order corrections lead to intriguing and peculiar effects that are relevant for systems including shallow water waves and optical media [2–6]. For example, the dynamics of shock waves in systems with higher-order dispersion have recently been investigated in Sprenger et al. [1] using a fifth-order Korteweg-deVries equation to describe classical shallow water waves. Due to the complexity of the dynamics, many open questions remain, and the fundamental nature of these shock waves is only starting to be explored.

Superfluids, such as dilute-gas Bose-Einstein condensates (BECs), provide a powerful platform for studying dispersive dynamics. By immersing a dilute-gas BEC into an appropriately tuned laser field generated by Raman beams, one can induce spin-orbit coupling (SOC) in the BEC [7]. This modifies the single-particle dispersion from parabolic, $E(p) = p^2/2m$, to a double-well structure with higher-order terms, similar in form to band structures found in condensed matter systems. Features of the dispersion can be tailored in experiments: for example, by changing the intensity of the Raman beams, one can manipulate the curvature of the dispersion.

A BEC with SOC constitutes an exotic medium through which topological defects, phonons, and shock waves can propagate. These features have characteristics that are strongly correlated with the properties of the underlying medium. For instance, in a conventional BEC, small-amplitude phonons propagate near the speed of sound in the medium at long wavelengths [8, 9], and as the wavelength decreases, the propagation speed increases slightly [10]. However, in a SOC BEC, the dispersion can be modified so that short wavelength modes travel more slowly in specific directions. This has a profound impact on the shape of

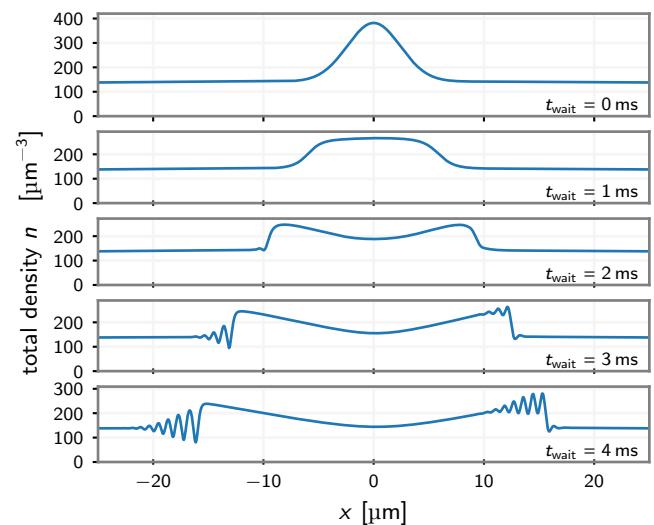


Figure 1. 1D numerical simulation modelling the development of dispersive shock waves in a SOC BEC. At $t_{\text{wait}} = 0$ ms, an initial density perturbation is formed by an attractive Gaussian potential at the center of the system. The potential is suddenly switched off at $t_{\text{wait}} = 0$ ms and the initial density perturbation spreads outwards ($t_{\text{wait}} = 1$ ms), forming two travelling peaks ($t_{\text{wait}} = 2$ ms) and developing into DSWs moving in opposite directions ($t_{\text{wait}} = 3$ and 4 ms). The structure of a DSW is highly dependent on the background dispersion. In a SOC BEC, the breaking of Galilean invariance induces two distinct DSW structures in a single system. To the right, the solitary wavetrain lags behind the solitary wave edge (shock front), while to the left, the solitary wavetrain travels faster than the large amplitude shock front.

dispersive shock waves (DSWs) that develop from non-linear interactions in the system [11]. A prototypical example of this is demonstrated in Fig. 1 showing the results of one-dimensional numerical simulations using realistic SOC parameters to form the single component dispersion, shown in Fig. 6.

Shock waves generated in a superfluid medium are typically

* m.forbes@wsu.edu

† engels@wsu.edu

considered to be dispersive: instead of becoming infinitely steep, the shock front is smoothed by gradients in the kinetic energy (dispersion). In direct contrast to this, classical shock waves are smoothed by dissipative effects such as viscosity. Depending on the amplitude of the excitations and the geometry of the system, shock waves in a superfluid can decay into a variety of intricate structures determined by the dimensionality of the system [12], in-part due to the presence of snaking instabilities along confined transverse directions [13–16]. In one-dimensional systems, effectively realized in elongated trap geometries with tight radial confinement, superfluid shock waves remain dispersive [10, 17, 18]. As the dynamics probe additional dimensions, however, shock waves can appear to be dissipative, despite a lack of dissipation in the superfluid systems [19, 20]. This effective viscosity arises from the generation of quantized superfluid vortices through snaking instabilities, resulting in a turbulent fluid that can be modelled by one-dimensional viscous shock wave (vsw) theory. We note that viscosity can appear in superfluids due to interactions with the normal component (mutual friction) and as intrinsic shear viscosity, but these effects are much smaller than those discussed here which can be reproduced with purely conservative simulations.

In this work, we showcase an example of the rich dynamics supported by superfluids with a higher-order dispersion. We experimentally demonstrate, with numerical verification, how DSWs evolve in a 3D SOC environment, resulting in asymmetric topological features displaying varying amounts of dissipation through viscous-like effects. Comparing with simulations, we interpret this viscous-like behavior as a manifestation of quantum turbulence arising from interactions of the shock front with vortex rings and solitons. The dynamics of these defects are subtly affected by the dispersion, resulting in qualitatively different macroscopic behavior. In this way, SOC provides a way to tune the effective viscosity of the macroscopic hydrodynamics realized in turbulent quantum fluids. This provides experimental control over cold-atom systems used as quantum simulators of turbulent hydrodynamics.

I. RESULTS

A. Experimental Setup

To investigate the excitation dynamics, we employ an elongated BEC of ^{87}Rb atoms, confined in an optical crossed-dipole trap [See Methods for detailed experimental parameters]. The BEC is cigar shaped with an aspect ratio of approximately 80:1, and the long axis of the BEC is oriented horizontally as shown in Fig. 2a. A uniform bias field in the z -direction splits the $F = 1$ hyperfine ground state in accordance to the Zeeman shift.

Spin-orbit coupling, with its associated double-well dispersion, is induced by applying two counter-propagating Raman beams that couple the $|F, m_F\rangle = |1, -1\rangle$ and $|1, 0\rangle$ state, which we designate as two spin orientations $|\uparrow\rangle$ and $|\downarrow\rangle$ of a pseudo-spin 1/2 system, respectively [see Fig. 2b and Methods]. The height of the central hump in the single-particle dispersion

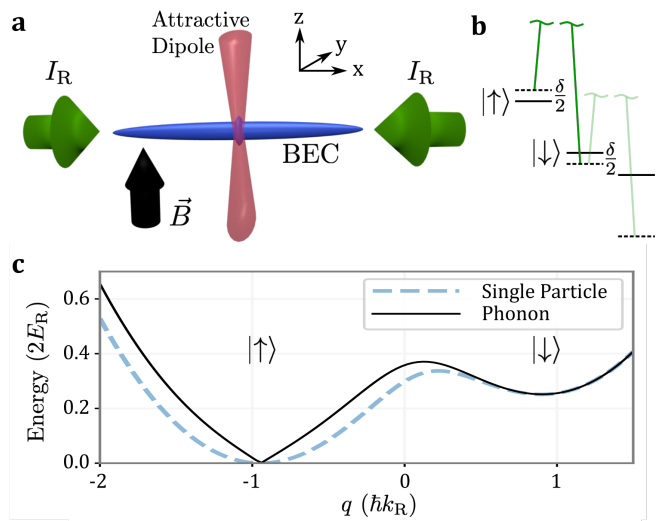


Figure 2. Experimental setup, level scheme and dispersion. **a** Experimental setup: an elongated BEC is prepared with spin-orbit coupling in the presence of a vertical magnetic field with two counter-propagating Raman beams (green). An attractive dipole sheet (red) is applied at the center of the BEC. **b** Relevant level scheme of the ^{87}Rb $|F = 1\rangle$ hyperfine states. The energies of the levels are shifted due to the Zeeman effect. Raman beams couple the $|\uparrow\rangle$ and $|\downarrow\rangle$ pseudo-spin states. **c** Two component excitation spectrum (black solid) and single particle dispersion (blue dashed) for the experimental parameters $\hbar\Omega = 1.5E_R$ and $\hbar\delta = 0.54E_R$. The blue-shaded area indicates quasimomenta with negative effective mass. The phonon dispersion has been shifted in the plot along the quasimomentum axis to line up with the single particle dispersion minimum for convenience.

(near quasimomentum $q = 0$ [see Fig. 2c]) depends on the Raman coupling strength Ω , which can be adjusted in the experiment by the intensity of the Raman beams, I_R . The energetic offset of the two local minima of the dispersion depends on the detuning δ of the Raman coupling, which can be set by the frequency difference between the two Raman beams. The experimentally realized single particle dispersion and the associated two-component phonon dispersion are shown in Fig. 2c by the dashed blue and solid black lines, respectively. See appendix D for more information. Energies and momenta are measured in units of the recoil energy, $E_R = \hbar^2 k_R^2 / 2m$, and recoil momentum, $k_R = 2\pi / \lambda_R$, where λ_R is the Raman laser wavelength. The BEC is prepared with SOC such that the majority amplitude of atoms are in the $|\uparrow\rangle$ spin state. The direction of SOC coincides with the long axis of the BEC such that the direction of positive quasimomentum $+q$ is in the $+x$ -direction, as indicated in Fig. 2a.

An additional dipole sheet aligned perpendicular to the long axis of the BEC creates an attractive Gaussian potential for the atoms at the center of the BEC. This vertical dipole sheet is pulsed on for 10 ms after the system has been prepared with SOC, resulting in excitations that propagate outwards along the long axis towards the edges of the BEC. The depth of this dipole potential U_b can be varied to generate large or small initial excitations in the BEC. In this work, U_b is on the order of the chemical potential of the majority component state ($|\uparrow\rangle$) in

the SOC BEC, μ . To analyze the dynamics, absorption imaging is performed after a 10.1 ms time-of-flight expansion. A Stern-Gerlach technique is used to vertically separate the spin states during the imaging procedure. Representative images obtained this way are presented in Fig. 3, where the $|\downarrow\rangle$ state is not shown due to very low number atoms in the minority component.

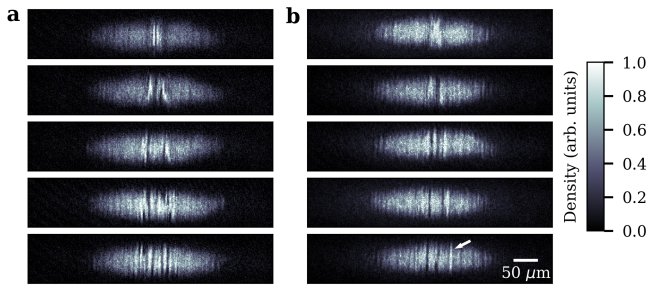


Figure 3. Experimental results with and without SOC. Absorption images acquired after a 10.1 ms time-of-flight expansion show the dynamics of outward moving excitations in a BEC prepared **a** without and **b** with SOC at times $t = 0, 4, 8, 12$ and 16 ms after a $U_b = -90$ nK $\approx -1.6\mu$ attractive potential has been applied for 10 ms. A Stern-Gerlach technique is used during time-of-flight to vertically separate the spin states in **b**, where only the majority component is shown. The arrow in the last panel of **b** indicates a highly reproducible peak propagating to the right that is discussed in the main text.

B. Experimental Results

We have performed a systematic study of the dynamics following the sudden switch-off of the dipole sheet as a function of the evolution time t_{wait} and initial potential strength U_b . A synopsis is presented in Fig. 4 and reveals the following features, the interpretation of which is confirmed by our matching numerical simulations: In the absence of SOC, the left-travelling and right-travelling excitations qualitatively behave the same as they propagate to the edges of the BEC, forming vortex rings and dark solitons. When strong SOC is applied to the system, parity is broken and an asymmetric behavior is observed between the two directions. This asymmetric behavior is highly dependent on the depth of the initial potential with respect to μ and on the coupling strength of the SOC. For a system where the SOC coupling strength Ω and detuning δ are fixed, the following behavior is found:

1. When $U_b < \mu$, excitations move outwards from the center of the BEC, displaying no discernible difference between the cases with and without SOC.
2. When $U_b \gtrsim \mu$, the excitation propagating to the right consistently forms a well-defined peak that becomes particularly pronounced during the expansion dynamics and travels outward from the center towards the right edge of the cloud at a relatively constant velocity. For clarity, this peak is indicated with a white arrow in the lower right image of Fig. 3. Quantitative analysis of the right-travelling excitation yield experimental speeds of

1.63 ± 0.04 mm/s for $U_b = -30$ nK, 1.64 ± 0.05 mm/s for $U_b = -60$ nK, and 1.68 ± 0.06 mm/s for $U_b = -90$ nK. This excitation is highly reproducible and observed to have a lifetime comparable to small-amplitude excitations in past phonon excitation experiments [9, 10, 18]. In addition, solitonic excitations are seen in the experimental images, and numerical simulations of the GPE identify the generation of a collection of defects, including solitons, solitonic vortices, and vortex rings, during the 10 ms pulse of the attractive potential. The positions of these features depend subtly on small details, such as a tiny tilt in the dipole sheet, which are expected to vary in the experiment from shot to shot.

C. Numerical Results

To understand the experimental results, numerical simulations of a coupled set of GPES are performed:

$$i\hbar \frac{\partial}{\partial t} \begin{pmatrix} |\uparrow\rangle \\ |\downarrow\rangle \end{pmatrix} = \begin{pmatrix} \frac{\hat{p}^2}{2m} + V_{\uparrow} & \frac{\Omega}{2} e^{2ik_R x} \\ \frac{\Omega}{2} e^{-2ik_R x} & \frac{\hat{p}^2}{2m} + V_{\downarrow} \end{pmatrix} \cdot \begin{pmatrix} |\uparrow\rangle \\ |\downarrow\rangle \end{pmatrix}, \quad (1a)$$

$$V_{\uparrow/\downarrow} = -\mu \pm \frac{\delta}{2} + g_{\uparrow\uparrow/\uparrow\downarrow} n_{\uparrow} + g_{\uparrow\downarrow/\downarrow\downarrow} n_{\downarrow} \quad (1b)$$

where $\hat{p} = -i\hbar\nabla$ is the momentum operator, μ is the chemical potential in the SOC system, $g_{ab} = 4\pi\hbar^2 a_{ab}/m$, and a_{ab} are the s -wave scattering lengths (with $a, b = \uparrow$ or \downarrow). For ^{87}Rb , $a_{\uparrow\uparrow} = 100.40a_0$, $a_{\downarrow\downarrow} = 100.86a_0$, and $a_{\uparrow\downarrow} = 100.41a_0$ where a_0 is the Bohr radius. The system is prepared in the ground state with a Thomas-Fermi (TF) cloud radius of $x_{\text{TF}} = 150\mu\text{m}$ along the long axis, corresponding to $N_{\uparrow} = 206000$ and $N_{\downarrow} = 6000$ atoms in the condensate. The SOC parameters are $\hbar\Omega = 1.5E_R$ and $\hbar\delta = 0.54E_R$. To reduce computational costs, cylindrical symmetry is employed about the long axis of the trap. The system is evolved in real time following the experimental protocol including the imaging procedure, which we implement in an expanding coordinates system as discussed in [21]. See appendix E for details. This introduces some significant artifacts by restricting vortices to be vortex rings, but allows us to fully simulate the experimental procedure including the expansion and imaging. Limited full 3D simulations of the in situ dynamics confirming the behavior discussed here are shown in Fig. 5.

D. Interpretation of Results

As demonstrated in the experimental absorption images Fig. 3, a striking effect of the modified dispersion is the apparent stabilization of the right-moving shock wave, leading to a highly reproducible peak seen in the expansion images that is traveling to the right. This feature is reproduced by our numerical simulations, allowing us to probe the microscopic mechanism for this stabilization. Our numerics are summarized in Fig. 5. Details and animations can be found in appendix F.

The numerics show the following progression of events. Shortly after turning on the attractive potential, fluid is drawn

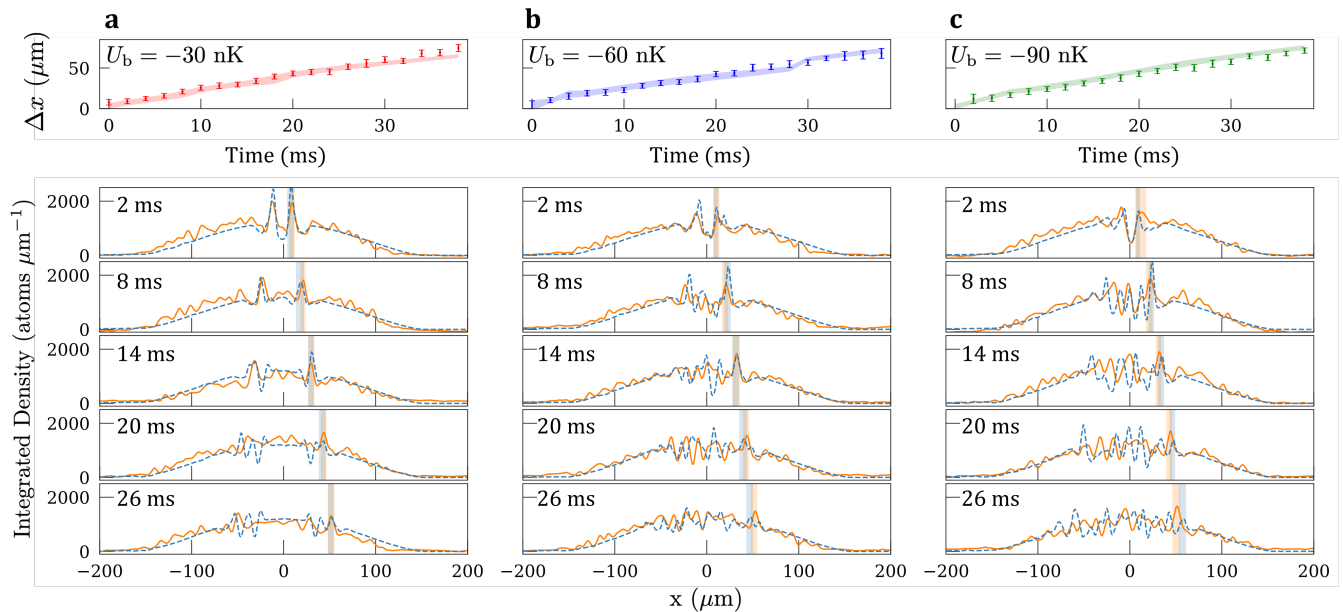


Figure 4. Experimental results and numerical simulations. Analysis and integrated cross sections of an expanded BEC prepared with SOC after an attractive potential with **a** $U_b = -30$ nK, **b** $U_b = -60$ nK, or **c** $U_b = -90$ nK has been pulsed on at the center of the cloud for 10 ms. After the potential is switched off, the system is allowed to evolve for a time t_{wait} in the presence of SOC prior to 10.1 ms time-of-flight expansion. The top row shows the position of the right moving excitation over time for GPE simulations (shaded region) and experiment (data points) for each potential depth, measured using a Gaussian fit function. The error bars and bands for both experiment and numerical results show the 2σ waist of the fitted Gaussian to the measured excitation. Quantitative results for the experiment are stated in the main text. In the lower panels, integrated cross sections for both GPE simulation (blue) and experiment (orange) are provided for each potential depth after $t_{\text{wait}} = 2, 8, 14, 20$ and 26 ms, where the shaded regions reflect the data presented in the top row. The GPE simulations presented here are performed using axial symmetry, which forces topological defects to align along the imaging axis. For more information, see [appendix D](#). The simulations have been modified to reflect the optical resolution of the experiment ($\sim 2 \mu\text{m}$) using a Gaussian convolution method.

into the central region of the trap where the potential is located ([Fig. 5a](#)). The subsequent flow induces a snaking instability [[13–16](#)] seen in [Fig. 5b](#), forming vortex rings on either side of the growing central excitation, or bulge. During the initial stages of evolution, vortex rings form quite symmetrically on both sides. Most have their central flow oriented towards the center of the cloud, however, with increasing barrier strength some vortex rings form with central flow facing outward.

After the attractive potential is turned off, the central bulge expands along the axis of the trap, as shown in [Fig. 5c](#). This can be described by decomposing the bulge as a superposition of left- and right-moving bulges (phonons), which move outward at approximately the local speed of sound once the attractive potential is suddenly switched off. Due to the non-linear interaction, these left- and right-moving bulges quickly form DSWs, the orientation and polarization [[22](#)] of which are sensitive to the curvature of the dispersion as shown in [Fig. 1](#). In particular, the left-moving DSW forms a leading soliton train as short-wavelength components travel faster than the solitary wave edge of the bulge. On the right, a small-wavelength soliton train trails behind the bulge. This has a simple explanation in terms of the modified dispersion. On the right, the phonon dispersion has negative curvature, and both group and phase velocities of the short-wavelength modes are *slower* [[1, 22](#)]. Discerning these features in an experiment would require high-resolution in-situ imaging as they are on the order of the healing length

and they do not survive the expansion imaging procedure.

As these outward traveling shock waves overtake the initially seeded vortex rings, intriguing dynamics ensue and a complex interaction develops between the rings and the shock front, as shown in [Fig. 5d](#). In particular, the vortices absorb energy and momentum from the shock front, causing the shock to dissipate as if it were a viscous shock wave (vsw) even though the total energy is conserved by the system. This is consistent with previous observations of vsws in superfluids as a result of dimensional reduction [[19, 20](#)] where a dissipationless superfluid in 3D is described by viscous hydrodynamics in 1D after integrating over the transverse directions. The modified dispersion plays an important role here, significantly suppressing these dissipative effects. In [Fig. 5d](#) one can see a large number of vortex rings on the left side of the cloud, while very few remain on the right. Examining the detailed dynamics (see the [appendix F](#)), we see that vortex-vortex and vortex-shock front interactions are more likely to trigger vortex annihilation on the right side of the cloud than on the left. As a result, fewer vortices remain on the right and less energy is dissipated from the shock front, leading to less effective viscosity and to the stabilization effect we observe in experiments with modified dispersion.

One might wonder if the asymmetry is due to the initial asymmetric form of the DSWs shown in [Fig. 1](#), in particular noting that the strong leading soliton train on the left might

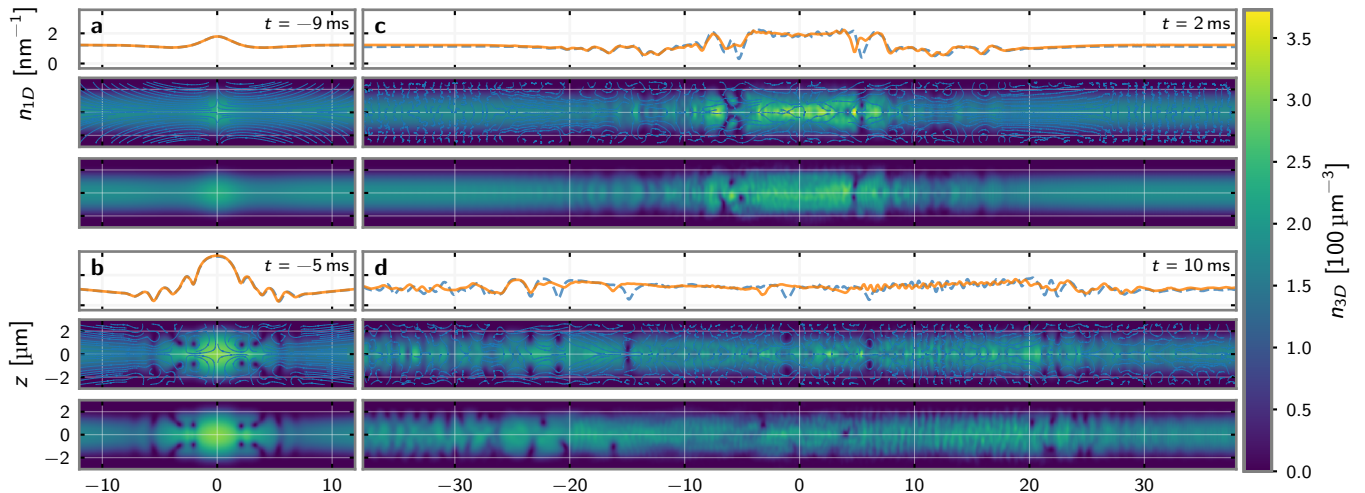


Figure 5. Numerical simulations with and without barrier tilt. Simulated in situ images (prior to the expansion) of the four distinct stages of evolution from a simulation of the experiment with a -60 nK attractive potential. Here we compare axially symmetric simulations to 3D simulations with a small 1% y -tilted Gaussian dipole beam $V_{DB} \propto \exp((x + 0.01y)^2/2\sigma)$. Upper frames are the integrated line-density $n_{1D}(x) = \int dydz n(x, y, z)$, with axially symmetric data (blue), and 3D tilted data (orange). Middle frames are slices $n_{3D}(x, y) = n(x, y, 0)$ for axially symmetric simulations with streamlines of the current density $n_{\uparrow}\vec{v}_{\uparrow} + n_{\downarrow}\vec{v}_{\downarrow}$. Bottom frames are slices $n_{3D}(x, y) = n(x, y, 0)$ from the 3D tilted simulations. **a** Initial flow of the BEC into the region of the attractive potential. **b** Formation of several vortex rings due to snaking instabilities induced by this flow. The pattern of rings here is quite symmetric, even in the tilted case. Vortex rings appear as reduced density in the 1D plots with mild dependence on the ring radius. **c** Formation of outgoing DSWS after the attractive potential is removed at $t = 10$ ms. In this frame, the DSWS are just starting to interacting with the first seeded vortex ring: without the seeding rings, the structure of these DSWS is similar to that shown in Fig. 1. In the tilted case, the vortex rings rapidly decay into vortices that break the axial symmetry and average to significantly smoother integrated line-density. **d** Results of DSWS interacting with initial vortex rings. Note that many fully-formed and stable vortices exist on the left, while fewer vortices survive on the right. This is attributed to an increased number of vortex annihilation events to the right, evident by the manifestation of short wavelength oscillations in the integrated cross sections. Some features are sensitive to the tilt, such as the vortices near $x = 0$ whose location shifts by several microns in the integrated 1D density. Others remain robust, such as the right-moving shock wave and corresponding peak at $20 \mu\text{m}$ to $25 \mu\text{m}$.

trigger the formation of more vortices. While this likely plays a role, it appears that the vortices seeded in Fig. 5d, Fig. 5b are crucial to the observed dynamics, at least at these potential strengths. Both numerics and experiment reveal that using a shallower potential, such as $U_b = -30$ nK (see Fig. 4a), decreases the number of vortices generated initially in the system, thus greatly reducing the effective viscosity, and shocks propagate in both directions without significant dissipation.

Explaining the exact microscopic mechanism for the enhanced likelihood of vortex annihilation with modified dispersion requires further investigation, but we anticipate that this is largely due to the presence of a modulational instability in the region of negative effective mass (shaded region in Fig. 2c) [23]. As the shock front passes through a vortex ring, it can induce portions of its flow to enter this region where modulational instabilities can manifest. Our numerics reveal that this often triggers the vortex ring to rapidly collapse or expand out of the system, effectively decaying to many high-frequency phonons seen as rapid, near-stationary oscillations on top of the simulations in Fig. 5d. In contrast, vortex interactions with the shock front moving to the left change the diameter of the vortex rings, triggering fewer annihilation events, and leaving them free to absorb the energy from the passing shock wave. Annihilations from the modulational instability occur primarily in the center

of vortex rings when the relative flow from the passing shock front increases the quasimomentum into the negative mass region. Notably, the rapid oscillations from the modulation instability are also seen developing on the cusp of the outward traveling right side DSW in the raw $U_b = -30, -60$ and -90 nK numerical data sets.

E. Expansion Dynamics

Structures induced by SOC and topological defects formed during DSW decay have length scales on the order of a healing length. These length scales are below the imaging resolution in our experimental setup. Therefore, time-of-flight imaging with 10.1 ms expansion time is used. During this expansion, features like solitons and vortices widen and thus can be resolved by the imaging system [24]. We have performed numerical simulations of the expansion dynamics which reveal that this process is nontrivial and the structures of the excitations change considerably during this time. We find that the expansion process significantly enhances the peak of the DSWS, allowing it to be clearly imaged after the experiment: After the BEC is released from the trap, the gas expands rapidly in the radial direction, reducing the density by more than a factor of 10 in

2 ms, and rendering the gas essentially non-interacting. In the remaining 8 ms of expansion, the various frequency components determined from the bare particle dispersion separate with velocity $v = \hbar k/m$, where k is the wave vector of the frequency component. What remains is a highly enhanced peak moving with the characteristic momentum of the shock wave. See [appendix G](#) for more information and animations.

II. DISCUSSION

Using an attractive dipole sheet to generate large amplitude excitations on the background of a SOC BEC, we are able to probe the effects of higher-order dispersion on the non-linear dynamics in an ultracold atomic system. The experimental results show a clear asymmetry in the non-linear dynamics in the presence of SOC, manifesting an enhanced stability of shock fronts propagating into the direction of higher-order dispersion, in agreement with GPE simulations. Within the numerical simulations, one is able to resolve the microscopic origin of this stability: the SOC significantly modifies the dynamics and stability of vortices in the region of modified dispersion, reducing their ability to dissipate energy from the shock wave. While it has been shown that the presence of SOC significantly alters the structure of vortices [25], no comparable study of the effect on their dynamics has been performed.

The left-moving shock front decays rapidly, leaving behind a wake of vortices, while the right-moving shock front remains quite stable. We interpret the observed asymmetry as a manifestation of quantum turbulence: Viewed in terms of 1D vsw theory, the vorticity induced in the system provides a mechanism to absorb energy, resulting in an effective viscosity in the 1D theory, similar to that seen in previous superfluid experiments [19, 20]. This effect is qualitatively consistent with our results, but further analysis is required to quantify the effective viscosity. In this language, the modified dispersion here significantly alters the vortex dynamics in comparison to previous cited works, reducing the effective viscosity for the right-moving shock front. Thus, SOC provides an effective tool for modifying the underlying dynamics of vortices, and thereby tuning the effective viscosity of the long-range hydrodynamic effective theory. Such control is essential for using cold-atoms as effective quantum simulators for turbulent fluid dynamics.

ACKNOWLEDGMENTS

We thank Prof. Mark Hofer and Patrick Sprenger for thoughtful and in-depth discussions concerning the behavior and shape of shock structures in higher-order dispersions. M.E.M. and P.E. are supported by the National Science Foundation (NSF) through Grants No. PHY-1607495 and PHY-1912540. E.S.D. and M.M.F. are supported by the NSF through Grant No. PHY-1707691.

Appendix A: Movies

The following are links to movies on YouTube showing various results:

Axial 30 nK, Axial 60 nK, Axial 90 nK: Axially symmetric simulations of the data in [Fig. 4](#), before time-of-flight (TOF) expansion.

Axial 90 nK ToF twait 26 ms: Axial simulation of 10.1ms TOF expansion starting after 26 ms in trap evolution.

Axial 3D tilt 30 nK: : A comparison between the Axial, tube, 3D, and 1% tilt 3D numerical methods at barrier depth -30 nK.

Appendix B: Experimental Methods and Parameters

Our experiments are conducted with elongated BECs of ^{87}Rb atoms. The atoms are confined in an optical crossed-dipole trap with trap frequencies $\{\omega_x, \omega_y, \omega_z\} = 2\pi \times \{3.49, 278, 278\}$ Hz, where the weakly confining direction is oriented horizontally. A 10 G uniform bias field leads to a Zeeman splitting of the hyperfine states. The $|1, -1\rangle$ and $|1, 0\rangle$ state are coupled through a two-photon Raman transition, while the $|1, +1\rangle$ state is essentially uncoupled due to the quadratic Zeeman effect. After loading into SOC, there are approximately 2×10^5 atoms in the majority ($|\uparrow\rangle$) component of the condensate. During the experiment, the Rabi coupling strength is $\hbar\Omega = 1.5E_R$. The detuning of the Raman drive is set to $\hbar\delta = 0.54(1)E_R \equiv 2000(50)$ Hz, where the uncertainty is given by the stability of the external bias field.

During the preparation and course of the experiment, heating caused by the Raman beams will decrease the condensate fraction, reducing the 1D longitudinal speed of sound and the equivalent non-SOC chemical potential in the majority component spin state from their initial values of $c_{s0} \approx 2.2$ mm/s and $\mu_0 \approx 100$ nK to $c_s \approx 1.6$ mm/s and $\mu \approx 55$ nK, respectively.

An additional vertical dipole sheet, with $\lambda_b = 850$ nm and Gaussian waists $\{w_x, w_y\} = \{4.8, 27.2\}$ μm , is focused onto the center of the BEC. The extent of the Gaussian profile in the y-direction is larger than the size of the BEC in-situ. The beam is pulsed on for 10 ms to create excitations at the center of the cloud.

Imaging is performed after 10.1 ms time-of-flight expansion during which all laser beams are off, and a Stern-Gerlach technique is used to vertically separate the spin states during the imaging procedure.

Appendix C: GPE Simulations

To model the experiment, we adjust the chemical potential μ so that the density of the gas vanishes at $x_{\text{TF}} = 150$ μm in the TF approximation. These parameters correspond to a lattice spacing of $dx \approx 0.06$ μm which is sufficiently small compared with the healing length $\xi \approx 0.22$ μm in the center of the cloud.

We start from the ground state in a harmonic trap with frequencies $\{\omega_x, \omega_y, \omega_z\} = 2\pi \times \{3.49, 278, 278\}$ Hz. We then evolve in real time using a 5th-order Adams-Bashforth-Milne (ABM) predictor-corrector integration scheme [26] with step size $dt = 6.3 \mu\text{s}$. We model the dipole sheet with a gaussian potential centered on x_0 with a width of $\sigma = 4.8 \mu\text{m}$. This potential is turned on and off smoothly using a C_∞ step function over $t_{\text{step}} = 0.1$ ms. We note that it is important for the accuracy of the ABM method that the time-dependent parameters vary smoothly.

To simulate the cloud expansion, we use the scaling procedure described in [21] to scale the radial coordinate without needing to add more lattice points to our simulation. Since the trapping potential along the cloud is weak, there is very little expansion along the cloud, so we do not scale the coordinate in this direction – our box is sufficiently large to accommodate this expansion.

Although the dynamics are three-dimensional, the two radial trapping frequencies are approximately equal, and the full 3D dynamics are well approximated by an axially symmetric geometry. Axially symmetric simulations can reproduce turbulent features generated by a quantum-mechanical piston in a channel geometry, like that found in Ref. [20]. Similar agreement between axially symmetric simulations [27] that can reproduce 3D shock phenomena in channel geometries [19] has also been observed in fermionic superfluids.

There are two differences of note between the experiment and GPE simulations. First, the numerical simulations enforce an axial symmetry, which restricts solitonic excitations, such as vortex rings, to be axially symmetric. While this is consistent with the experimental geometry, it is well known that small perturbations will destabilize vortex rings, which can evolve relatively quickly into solitonic vortices [15, 16, 28–34]. We have verified by performing unrestricted 3D simulations (see the appendix G) that perturbations as small as 1% in alignment of the dipole beam (see the third panel of Fig. 5) rapidly induce these instabilities, resulting in much smoother average densities on the left consistent with the experimental images, but performing full high-resolution simulations for direct comparison is prohibitive for this initial study. We therefore expect that where the simulations produce vortex rings, we can expect to observe solitonic vortices in the experiment. Despite these radial instabilities, we have verified that using axially symmetric simulations still quantitatively reproduces the bulk dynamics in these elongated systems.

Second, while preparing the SOC BEC in the experiment, a thermal cloud is generated by the Raman beams in the initial state. This is observed in 1D cross sections of the data. While in principle one can include the effects of the thermal cloud using the stochastic projected Gross-Pitaevskii Equation (SPGPE) [35–38] or Zaremba-Nikuni-Griffin (ZNG) [39, 40] formalisms, the agreement between our simulations and experiment show that these effects are small.

Appendix D: SOC Phonon Dispersion

In a previous work, Khomehchi et al. used a single-particle dispersion to describe the expansion of a SOC BEC into a vacuum, notably matching the speed and DSW shape during expansion [23]. In this work, the DSW is expanding through a non-zero background density. From this perspective, DSWs are large amplitude phonons described by a phonon dispersion constructed from Bogoliubov-de Gennes (BdG) theory. For a SOC BEC, this theory predicts linear dispersion for small phonon momenta and a roton-like branch at large phonon momenta. This assumes a one-component phonon model. To capture the full physics in the regions of negative mass, a two-component model is required.

In this work, we maintain both components as the single-band model does not correctly reproduce the phonon dispersion in the presence of the superfluid background with SOC (see Fig. 6). Including the second component shifts the dispersion to a lower energy in the negative mass region, resulting in slower DSW propagation in the $+q$ -direction.

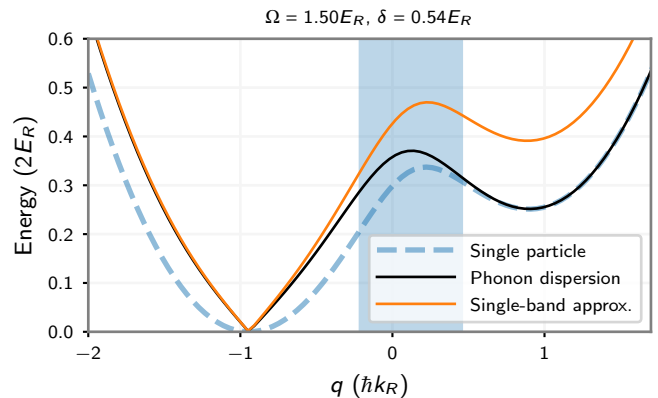


Figure 6. Phonon dispersions with SOC. Phonon dispersion (solid) for the full theory (thick black curve) compared with the single-band approximation Eq. (D1) (thin orange curve) and single-particle dispersion (blue dashed) for experimental parameters $\hbar\Omega = 1.5E_R$ and $\hbar\delta = 0.54E_R$. The blue-shaded area indicates quasimomenta with negative effective mass. The phonon dispersion has been shifted to line up with the single particle dispersion minimum for convenience. While qualitatively similar, the single-band model has some quantitative differences. For this reason, we simulate the full two-component model in all of our results.

The two-component, single-band model of the GPE is given by

$$i\hbar \frac{\partial}{\partial t} |\psi\rangle = [E_-(\hat{p}) + gn + V_{\text{ext}}(x)] |\psi\rangle, \quad (\text{D1})$$

where $E_-(\hat{p})$ is the dispersion of the lower band obtained by diagonalizing equation (1) for homogeneous states. Here $|\psi\rangle$ is the wavefunction corresponding to the eigenstate of equation (1) describing the lowest band, and is a linear combination of the two bare hyperfine states. For inhomogeneous densities this picture is locally valid for slowly varying densities, similar to the Thomas-Fermi approximation, and remains valid as long as the

system is gently excited compared to the band separation, which is proportional to the strength Ω of the Raman coupling. With our parameters, the single-band model exhibits qualitatively similar results to the multi-band description, reproducing many aspects of the experiment, but shows quantitative differences. The approximate equality of the coupling constants allows one to define a spin-quasimomentum mapping that relates the two-component spin populations n_\uparrow and n_\downarrow to the quasimomentum q of the single-component state:

$$\frac{n_\downarrow - n_\uparrow}{n_\downarrow + n_\uparrow} = \frac{k - d}{\sqrt{(k - d)^2 + w^2}}, \quad (\text{D2})$$

where we have defined the dimensionless parameters $k = p/\hbar k_R$, $d = \delta/4E_R$, and $w = \Omega/4E_R$. This simplified model captures the interesting phenomena observed in the experiment, but is not quantitatively accurate.

Appendix E: Axially Symmetric GP Simulations

In Fig. 4 of the main text, experimental results are directly compared to a 1D Gaussian convolution (mimicking the optical resolution of the experiment) of axially symmetric numerical GPE simulations. In this figure, the simulations show significant peaks moving to the left that are not observed in the experiments. This is due to the restricted axial symmetry in the simulations, forcing all defects to be aligned along the imaging axis. Symmetry unrestricted simulations show that small perturbations cause these defects to align quasi-randomly, averaging out and only the shock fronts remains. 3D simulations are computationally expensive to perform for the full system, and while they are able to show an accurate picture of the experimentally observed dynamics, 2D axially symmetric numerical simulations are able to reproduce some of the key macroscopic features observed in experiments.

The simulations in Fig. 4 were made using the axially symmetric GPE with a $N_x = 8000$ by $N_r = 50$ grid, a Thomas Fermi radius of $x_{TF} = 150 \mu\text{m}$, and the barrier depths -30 nK , -60 nK , and -90 nK , respectively.

The simulated data in [Axial 30 nK](#), [Axial 60 nK](#), and [Axial 90 nK](#) show detailed dynamics of the system in three time regimes: First, from $t_{\text{wait}} = -10 \text{ ms}$ to 0 ms , showing the dynamic generation of turbulent features; second, from $t_{\text{wait}} = 0 \text{ ms}$ to 6 ms , showing the interaction between the DSW and the turbulent features stabilizing the right-hand side shock wave; third, from $t_{\text{wait}} = 6 \text{ ms}$ onward, showing the motion of the turbulent features once the density peak has passed.

The attractive potential is turned on at $t_{\text{wait}} = -10 \text{ ms}$ and the superfluid floods into the barrier, forming a large peak in the center. Within 2 ms, areas of modulated density form grey solitons at the edges of barrier. For shallow barriers (-30 nK) these solitons are stable. However, for larger barriers (-60 nK and -90 nK) a snaking instability sets in, nucleating vortex rings that appear as vortex anti-vortex pairs in an axial simulations. The vortex rings form mostly with their central flow oriented away from the center of the cloud. This is clearly seen in the -30 nK simulation where all the vortex ring have a

net outward flow and move in that direction. For larger potential heights, vortex rings of opposite orientation also form.

The vortex rings move according to the Magnus relation $\vec{v} \propto \vec{k} \times \vec{F}$, where \vec{v} is the velocity of the vortex, \vec{k} is the circulation of the vortex, and \vec{F} is a force acting on the vortex. If a vortex ring experiences a force in the same direction as its central flow, it will expand. A vortex ring experiencing a force in the opposite direction to its central flow will shrink. In the present setting, the vortex rings see a flow towards the attractive potential (altering \vec{v}) and a density gradient from the density peak ($\vec{F} = -\nabla gn$) which expands rings that are orientated away from density peak and shrinks rings that are orientated towards it. For larger potential heights, non-equilibrium dynamics, including vortex ring collisions and annihilations, distort these features.

The attractive potential is turned off in 0.1 ms and at $t_{\text{wait}} = 0 \text{ ms}$ is completely off as the central density peak expands outward, pushing past the turbulent features. The density gradient widens (shrinks) vortex rings of same (opposite) central flow. If a ring becomes too small, it will annihilate through a Jones-Robert soliton [41–44]. Vortex rings with central flow oriented towards the SOC have a larger phase space to annihilate, leading to less vorticity, less effective viscosity, and less dissipation on the right hand side.

A closer look at the individual components around a vortex ring shows that areas with flow in the direction of the SOC have higher densities of $|\downarrow\rangle$. As the density peaks pass through the vortex rings, the bump moving in the direction of the SOC converts particles from $|\uparrow\rangle$ to $|\downarrow\rangle$, while the bump traveling in the opposite direction converts particles from $|\downarrow\rangle$ to $|\uparrow\rangle$. For wait times longer than $t_{\text{wait}} = 8 \text{ ms}$, the density bumps have developed DSW structures and the remaining vortex rings move according to the Magnus relation expected from their flow.

In Fig. 4b at $t_{\text{wait}} = 20$ and 26 ms, as the large excitation moves through a vortex ring the integrated density appears as a double peaked intensity. This causes the tracked excitation peak in the top panel of Fig. 4b to appear kinked in the numerical (blue shaded) results.

Appendix F: Axial versus 3D Numerics

Due to the computational memory needed for full 3D calculations, the BEC is modelled in a smaller box, with $L_x = 120 \mu\text{m}$, $N_{xyz} = (1200, 64, 64)$, and a periodic trapping potential. This reduces the memory costs by a factor of 4, and is accurate for short times and dynamics in the center of the cloud. Similarly, in some cases, a quasi-1D simulation using techniques like the non-polynomial Schrödinger equation (NPSE) [33, 45–47] and dynamically rescaled GPE (GPE) [48] can quantitatively reproduce the 3D dynamics. However, these are insufficient once features like vortices appear, as shown in [49].

Comparing 3D to axially-symmetric simulations in [Axial 3D tilt 30 nK](#), we see almost exact agreement during the 10 ms long attractive potential pulse. This includes the formation of solitons, vortices pulled in from the boundary, and the snaking creation of vortex rings. The simulations differ as the density peak splits and pushes past the central vortices: the 3D

simulations allow for more vortices to remain. However, there is agreement between the shape and speed of the DSWs, and the speed of solitonic and vortex features. We have verified that 3D simulations are required to qualitatively explain the observed behavior.

To test the stability of vortex rings against small changes of the experimental parameters, we simulated the attractive dipole beam with a 1% tilt in the y -direction, $V_{DB} \propto \exp((x + 0.01y)^2/2\sigma)$. In this data (Fig. 5 third panel) and supplementary animations, we see that main features like the DSW maintain their structure. However, many of the vortex rings decay in to vortex lines that terminate at cloud edge.

Appendix G: Time-of-Flight dynamics

The technique used to numerically simulate the expansion of the system during the 10.1 ms time-of-flight corresponds to setting $\lambda_1(t) = 1$ and $\lambda_2(t) = \lambda_3(t) = \lambda_{\perp}(t)$ in Eqs. (11) and (15) of Ref. [21]. The evolution of dynamics during time-of-flight is shown in [Axial 90 nK ToF twait 26 ms](#)

When the Raman lasers inducing the SOC are switched off, the system is projected into the undressed basis of states $|\uparrow\rangle$ and $|\downarrow\rangle$. Without SOC to dress their momenta, the $|\uparrow\rangle$ component moves slowly to the right while the $|\downarrow\rangle$ component moves rapidly to the left, making it difficult to locate the center of the cloud. This can be understood in terms of the background ground state which is a linear combination of mostly $|\uparrow\rangle$ (with density n_{\uparrow}) having momentum $k_{\uparrow} = k_0 + k_R$ and some $|\downarrow\rangle$ (with density n_{\downarrow}) having momentum $k_{\downarrow} = k_0 - k_R$. The spin-quasimomentum map ensures that the background has zero net momentum: $n_{\uparrow}k_{\uparrow} + n_{\downarrow}k_{\downarrow} = (n_{\uparrow} + n_{\downarrow})k_0 + (n_{\uparrow} - n_{\downarrow})k_R = 0$. With our detuning, $n_{\uparrow} > n_{\downarrow}$ and $k_0 \approx -0.945k_R$. Thus, during expansion, the two components move in opposite horizontal directions in addition to the vertical separation from the Stern-Gerlach technique. Within the first 2 ms of expansion the cloud expands rapidly, dropping the density by a factor of 10. The most notable features after expansion come from low density objects such as solitons, vortex rings, and DSW where areas with these features deepen and widen, pushing density to either side. The density pile-up of nearby vortex rings will often constructively interfere, resulting in some of the largest peaks during expansion dynamics.

-
- [1] P. Sprenger and M. A. Hofer, “Shock waves in dispersive hydrodynamics with nonconvex dispersion,” *SIAM Journal on Applied Mathematics* **77**, 26–50 (2017).
 - [2] A. Mohamadou, C. G. LatchioTiofack, and Timoléon C. Kofané, “Wave train generation of solitons in systems with higher-order nonlinearities,” *Phys. Rev. E* **82**, 016601 (2010).
 - [3] Stefania Malaguti, Matteo Conforti, and Stefano Trillo, “Dispersive radiation induced by shock waves in passive resonators,” *Opt. Lett.* **39**, 5626–5629 (2014).
 - [4] G. A. El and N. F. Smyth, “Radiating dispersive shock waves in non-local optical media,” *Proc. R. Soc. A* **472**, 1–21 (2016).
 - [5] Mulong Liu, Leiran Wang, Qibing Sun, Siqi Li, Zhiqiang Ge, Zhizhou Lu, Chao Zeng, Guoxi Wang, Wenfu Zhang, Xiaohong Hu, and Wei Zhao, “Influences of high-order dispersion on temporal and spectral properties of microcavity solitons,” *Opt. Express* **26**, 16477–16487 (2018).
 - [6] Yun Zhao, Xingchen Ji, Bok Young Kim, Prathamesh S. Donvalkar, Jae K. Jang, Chaitanya Joshi, Mengjie Yu, Chaitali Joshi, Renato R. Domenegueti, Felipe A. S. Barbosa, Paulo Nussenzveig, Yoshitomo Okawachi, Michal Lipson, and Alexander L. Gaeta, “Visible nonlinear photonics via high-order-mode dispersion engineering,” *Optica* **7**, 135–141 (2020).
 - [7] Y.-J. Lin, R. L. Compton, A. R. Perry, W. D. Phillips, J. V. Porto, and I. B. Spielman, “Bose-Einstein condensate in a uniform light-induced vector potential,” *Phys. Rev. Lett.* **102**, 130401 (2009).
 - [8] N. N. Bogoliubov, “On the theory of superfluidity,” *J. Phys. (Moscow)* **11**, 23–32 (1947).
 - [9] M. R. Andrews, D. M. Stamper-Kurn, H.-J. Miesner, D. S. Durfee, C. G. Townsend, S. Inouye, and W. Ketterle, “Propagation of sound in a Bose-Einstein condensate,” *Phys. Rev. Lett.* **79**, 553–556 (1997).
 - [10] J. J. Chang, P. Engels, and M. A. Hofer, “Formation of dispersive shock waves by merging and splitting Bose-Einstein condensates,” *Phys. Rev. Lett.* **101**, 170404 (2008).
 - [11] M. A. Hofer, M. J. Ablowitz, I. Coddington, E. A. Cornell, P. Engels, and V. Schweikhard, “Dispersive and classical shock waves in Bose-Einstein condensates and gas dynamics,” *Phys. Rev. A* **74**, 023623 (2006).
 - [12] P. G. Kevrekidis, D. J. Frantzeskakis, and R. Carretero-González, *The Defocusing Nonlinear Schrödinger Equation*, Other Titles in Applied Mathematics (Society for Industrial and Applied Mathematics, 2015).
 - [13] E.A. Kuznetsov, A.M. Rubenchik, and V.E. Zakharov, “Soliton stability in plasmas and hydrodynamics,” *Physics Reports* **142**, 103 – 165 (1986).
 - [14] A. Muryshv, G. V. Shlyapnikov, W. Ertmer, K. Sengstock, and M. Lewenstein, “Dynamics of dark solitons in elongated Bose-Einstein condensates,” *Phys. Rev. Lett.* **89**, 110401 (2002).
 - [15] Joachim Brand and William P. Reinhardt, “Solitonic vortices and the fundamental modes of the “snake instability”: Possibility of observation in the gaseous Bose-Einstein condensate,” *Phys. Rev. A* **65**, 043612 (2002), arXiv:cond-mat/0105581 [cond-mat.soft].
 - [16] M. A. Hofer and B. Ilan, “Onset of transverse instabilities of confined dark solitons,” *Phys. Rev. A* **94**, 013609 (2016).
 - [17] M. A. Hofer, P. Engels, and J. J. Chang, “Matter-wave interference in Bose-Einstein condensates: A dispersive hydrodynamic perspective,” *Physica D* **238**, 1311–1320 (2008).
 - [18] R. Meppelink, S. B. Koller, J. M. Vogels, P. van der Straten, E. D. van Ooijen, N. R. Heckenberg, H. Rubinsztein-Dunlop, S. A. Haine, and M. J. Davis, “Observation of shock waves in a large Bose-Einstein condensate,” *Phys. Rev. A* **80**, 043606 (2009).
 - [19] J. A. Joseph, J. E. Thomas, M. Kulkarni, and A. G. Abanov, “Observation of Shock Waves in a Strongly Interacting Fermi Gas,” *Phys. Rev. Lett.* **106**, 150401 (2011).
 - [20] M. E. Mossman, M. A. Hofer, K. Julien, P. G. Kevrekidis, and P. Engels, “Dissipative shock waves generated by a quantum mechanical piston,” *Nature Comm.* **9**, 4665 (2018).
 - [21] Y. Castin and R. Dum, “Bose-Einstein condensates in time dependent traps,” *Phys. Rev. Lett.* **77**, 5315–5319 (1996).

- [22] G. A. El and M. A. Hoefer, “Dispersive shock waves and modulation theory,” *Physica D* **333**, 11–65 (2016), [arXiv:1602.06163](#).
- [23] M. A. Khamehchi, Khalid Hossain, M. E. Mossman, Yongping Zhang, Thomas Busch, Michael McNeil Forbes, and Peter Engels, “Negative mass hydrodynamics in a spin-orbit-coupled Bose-Einstein condensate,” *Phys. Rev. Lett.* **118**, 155301 (2017), [arXiv:1612.04055](#).
- [24] B. P. Anderson, P. C. Haljan, C. A. Regal, D. L. Feder, L. A. Collins, C. W. Clark, and E. A. Cornell, “Watching dark solitons decay into vortex rings in a bose-einstein condensate,” *Phys. Rev. Lett.* **86**, 2926–2929 (2001).
- [25] J. Radić, T. A. Sedrakyan, I. B. Spielman, and V. Galitski, “Vortices in spin-orbit-coupled bose-einstein condensates,” *Phys. Rev. A* **84**, 063604 (2011).
- [26] Richard W. Hamming, *Numerical Methods for Scientists and Engineers* (McGraw-Hill, Inc., New York, NY, USA, 1973).
- [27] F. Ancilotto, L. Salasnich, and F. Toigo, “Shock waves in strongly interacting Fermi gas from time-dependent density functional calculations,” *Phys. Rev. A* **85**, 063612 (2012), [arXiv:1206.0568](#).
- [28] C. Becker, K. Sengstock, P. Schmelcher, P. G. Kevrekidis, and R. Carretero-Gonzalez, “Inelastic Collisions of Solitary Waves in Anisotropic Bose-Einstein Condensates: Sling-Shot Events and Expanding Collision Bubbles,” *New J. Phys.* **15**, 113028 (2013), [arXiv:1308.2994](#).
- [29] Matthew D. Reichl and Erich J. Mueller, “Vortex Ring Dynamics in Trapped Bose-Einstein Condensates,” *Phys. Rev. A* **88**, 053626 (2013), [arXiv:1309.7012](#).
- [30] Mark J. H. Ku, Wenjie Ji, Biswaroop Mukherjee, Elmer Guardado-Sanchez, Lawrence W. Cheuk, Tarik Yefsah, and Martin W. Zwierlein, “Motion of a Solitonic Vortex in the BEC-BCS Crossover,” *Phys. Rev. Lett.* **113**, 065301 (2014), [arXiv:1402.7052 \[cond-mat.quant-gas\]](#).
- [31] Gabriel Wlazłowski, Aurel Bulgac, Michael McNeil Forbes, and Kenneth J. Roche, “Life cycle of superfluid vortices and quantum turbulence in the unitary Fermi gas,” *Phys. Rev. A* **91**, 031602(R) (2015), [arXiv:1404.1038 \[cond-mat.quant-gas\]](#).
- [32] Peter Scherpelz, Karmela Padavić, Adam Raçon, Andreas Glatz, Igor S. Aranson, and K. Levin, “Phase Imprinting in Equilibrating Fermi Gases: The Transience of Vortex Rings and Other Defects,” *Phys. Rev. Lett.* **113**, 125301 (2014), [arXiv:1401.8267](#).
- [33] A. Muñoz Mateo and J. Brand, “Chladni solitons and the onset of the snaking instability for dark solitons in confined superfluids,” *Phys. Rev. Lett.* **113**, 255302 (2014).
- [34] Mark J. H. Ku, Biswaroop Mukherjee, Tarik Yefsah, and Martin W. Zwierlein, “From planar solitons to vortex rings and lines: Cascade of solitonic excitations in a superfluid Fermi gas,” *Phys. Rev. Lett.* **116**, 045304 (2015), [arXiv:1507.01047](#).
- [35] C. W. Gardiner, J. R. Anglin, and T. I. A. Fudge, “The stochastic Gross-Pitaevskii equation,” *J. Phys. B* **35**, 1555 (2002), [arXiv:cond-mat/0112129](#).
- [36] C. W. Gardiner and M. J. Davis, “The stochastic Gross-Pitaevskii equation: II,” *J. Phys. B* **36**, 4731 (2003), [arXiv:cond-mat/0308044](#).
- [37] S. J. Rooney, P. B. Blakie, and A. S. Bradley, “Stochastic projected Gross-Pitaevskii equation,” *Phys. Rev. A* **86**, 053634 (2012), [arXiv:1210.0952 \[cond-mat.quant-gas\]](#).
- [38] S. J. Rooney, P. B. Blakie, and A. S. Bradley, “Numerical method for the stochastic projected Gross-Pitaevskii equation,” *Phys. Rev. E* **89**, 013302 (2014).
- [39] E. Zaremba, T. Nikuni, and A. Griffin, “Dynamics of trapped Bose gases at finite temperatures,” *J. Low Temp. Phys.* **116**, 277–345 (1999).
- [40] A. J. Allen, C. F. Barenghi, N. P. Proukakis, and E. Zaremba, “A dynamical self-consistent finite temperature kinetic theory: The ZNG scheme,” in *Quantum Gases: Finite Temperature and Non-Equilibrium Dynamics*, Cold Atoms, Vol. 1, edited by Nick Proukakis, Simon Gardiner, Matthew Davis, and Marzena Szymańska (World Scientific, 2012) p. 93, [arXiv:1206.0145](#).
- [41] P. H. Roberts and J. Grant, “Motions in a Bose condensate. i. the structure of the large circular vortex,” *J. Phys. A* **4**, 55 (1971).
- [42] C A Jones and P H Roberts, “Motions in a Bose condensate. IV. Axisymmetric solitary waves,” (1982).
- [43] G. C. Katsimiga, S. I. Mistakidis, G. M. Koutentakis, P. G. Kevrekidis, and P. Schmelcher, “Many-body dissipative flow of a confined scalar Bose-Einstein condensate driven by a Gaussian impurity,” *Phys. Rev. A* **98**, 013632 (2018).
- [44] W. L. Wang, P. G. Kevrekidis, and E. Babaev, “Ring dark solitons in three-dimensional Bose-Einstein condensates,” *Phys. Rev. A* **100**, 053621 (2019).
- [45] A. Muñoz Mateo and V. Delgado, “Effective mean-field equations for cigar-shaped and disk-shaped bose-einstein condensates,” *Phys. Rev. A* **77**, 013617 (2008).
- [46] A. Muñoz Mateo and V. Delgado, “Effective one-dimensional dynamics of elongated bose-einstein condensates,” *Annals of Physics* **324**, 709 – 724 (2009).
- [47] A. Muñoz Mateo and V. Delgado, “Accurate one-dimensional effective description of realistic matter-wave gap solitons,” *J. Phys. A* **47** (2014), [10.1088/1751-8113/47/24/245202](#).
- [48] Pietro Massignan and Michele Modugno, “One-dimensional model for the dynamics and expansion of elongated bose-einstein condensates,” *Phys. Rev. A* **67**, 023614 (2003).
- [49] N. K. Lowman and M. A. Hoefer, “Fermionic shock waves: Distinguishing dissipative versus dispersive regularizations,” *Phys. Rev. A* **88**, 013605 (2013).